PAPER

Check for updates

Numerical evaluation of bi-facial ZnO/MoTe2 photovoltaic solar cells with N-doped Cu2O as the BSF layer for enhancing V_{OC} via device simulation†

Arifuzzaman Rajib, [ID] *[a] Tapos Chandra Saha, [ID] [a] Md. Mustafizur Rahman, [ID] [a] Hridoy Sarker, [ID] [a] Ruddro Dhali, [ID] [a] Md. Sabbir Hossain Sumon[a] and Atowar Rahman*[b]

Molybdenum telluride (MoTe2) shows great promise as a solar absorber material for photovoltaic (PV) cells owing to its wide absorption range, adjustable bandgap, and lack of dangling bonds at the surface. In this research, a basic device structure comprising Pt/MoTe2/ZnO/ITO/Al was developed, and its potential was assessed using the SCAPS-1D software. The preliminary device exhibited a photovoltaic efficiency of 23.87%. The integration of a 100 nm thick nitrogen-doped copper oxide (N-doped Cu2O) layer as a hole transport/BSF layer improved the device performance of the MoTe2/ZnO photovoltaic solar cell (PVSC), increasing the open circuit voltage (V_{OC}) from 0.68 V to 1.00 V and, consequently, its efficiency from 23.87% to 34.45%. Recombination and C–V analyses were conducted across various regions of the device with and without the BSF layer. The results of these analyses revealed that this improvement in the device performance mainly stemmed from a decrease in recombination losses at the absorber/BSF interface and an increase in the built-in potential of the device, resulting in improved V_{OC} and photovoltaic efficiency. Additionally, the performance of the device in a bifacial mode was studied. The calculated bifacial factor (BF) values suggested that there were negligible additional losses affecting some parameters when the solar cell was under backside illumination and emphasized the potential for improved energy harvest in bifacial solar cells without significant drawbacks.

1. Introduction

Energy from non-renewable energy sources increases the temperature of the earth by the emission of SO_2, CO_2, and CH_4 gases.[1] The use of renewable resources, such as sunlight and wind, must be increased in order to bring down fossil fuel consumption. The relentless pursuit of sustainable energy sources has propelled significant advancements in the field of solar energy. Different technologies have been applied to utilize solar energy, but photovoltaic (PV) cells have received considerable attention from researchers due to their cost-effectiveness and availability.[2–5] Nowadays, silicon-based solar cells dominate about 95% of the worldwide solar market. However, silicon (Si) possesses an indirect type bandgap, and its optical absorption is not as suitable as those of direct bandgap semiconductor

materials. Industrial production of silicon wafers requires temperatures of about 1400 °C, and thick wafers are often used for commercial purposes, which increases costs and the amount of materials used.[6–8] TFSCs have achieved notable progress in recent years, leading to the enhancement of cell performance and cost-effectiveness. TFSCs use a much thinner layer of semiconductor material in comparison with conventional silicon solar cells, making them cost-effective, lighter, and more flexible. The 2nd generation TFSCs are based on CdTe, CIGS, and lead chalcogenide PbX (X = S, Se). These are all direct bandgap semiconductors and have received considerable attention because of their exceptional performance in PV applications.[9–12] High production costs, *i.e.*, expensive materials and manufacturing processes associated with these technologies, primarily limit the commercialization of the 2nd generation TFSCs. Additionally, efficiency, reliability, and toxicity issues have hindered their widespread adoption in the market. These technologies have not yet achieved the same level of efficacy and long-term reliability as silicon-based solar cells, making them less attractive to commercial developers and investors.

To overcome these challenges, researchers have turned to earth-abundant, inexpensive, and eco-friendly materials like transition metal dichalcogenides (TMDCs) as the main

[a]Department of Electrical and Electronic Engineering, Bangabandhu Sheikh Mujibur Rahman Science and Technology University, Gopalganj, 8100, Bangladesh. E-mail: rajib.apee.38@gmail.com; rajib.eee@bsmrstu.edu.bd

[b]Department of Electrical and Electronic Engineering, University of Rajshahi, Rajshahi, 6205, Bangladesh. E-mail: atowar@ru.ac.bd

† Electronic supplementary information (ESI) available: Measurement procedures for recombination coefficient and surface recombination velocity details are available upon request. See DOI: https://doi.org/10.1039/d4ra05974c

absorber layer in solar cells. These materials exhibit excellent optical, mechanical, thermal, and electrochemical properties.[13–16] TMDCs have a three-layer chalcogenide-transition metal-chalcogenide microstructure, in which very weak van der Waals forces form bonds between the layers. Therefore, doping can be easily achieved in order to tune their electrical and optical properties.[17] Among the TMDCs, $MoTe_2$ has garnered considerable attention as a promising absorber material for thin-film solar cells because it exhibits a p-type behavior with exceptional optoelectronic properties.[18] In addition, it shows a bandgap in the range of 1 to 1.2 eV, superior optical absorption of $\sim 10^5$ cm^{-1}, and excellent carrier mobility.[19] Very recently, the photovoltaic solar cell with perovskite as an absorber layer has been in focus due to its high band gap, high efficiency, and excellent stability.[20–22]

However, $MoTe_2$ has not been explored well as an active layer for PV cells. In a recent study, a device structure of $Cu_2O/MoTe_2/$ CdS showed a PV performance of 32.38% power conversion efficiency (PCE).[19] However, toxic materials, such as cadmium, were used as window layers.[19] In another study, a $MoTe_2/n$-$MoSe_2$ PV cell structure showed a cell performance of 26.97% PCE, which further improved to 28.75% PCE using a heavily doped N-doped Cu_2O BSF layer.[23] However, it is worth noting that the BSF layer is inefficient as most of the sunlight photons are absorbed by the $MoSe_2$ window layer due to its very high absorption coefficient of $\sim 10^6$ cm^{-1} and moderate bandgap E_g of ~ 1.25 eV.[24–27] Therefore, very few photons are reflected by the BSF layer. TFSCs can be fabricated using various methods, each with distinct advantages and applications, including sputtering, CVD, PVD, ALD, PLD, and epitaxial growth. Epitaxy, which achieves high crystallographic alignment between the deposited film and substrate lattice, employs techniques such as MBE, epitaxial CVD, and atomic layer epitaxy (ALE). Data in Table 1 indicates that the lattice mismatch at the $ZnO/MoTe_2$ interface is 8.25%, while it is 19.43% at the $MoTe_2/N$-doped Cu_2O interface. This information aids in selecting an appropriate epitaxial growth technique for fabricating the proposed device structure with optimal crystallographic alignment among the layers.

These results suggest that PVSCs with $MoTe_2$ as an absorber layer have great potential to produce non-toxic, low-cost, and high-performance PVSCs. However, the choice of the window layer is crucial. However, ZnO is a promising material as a window layer for its widespread use in Cu_2O, c-Si, GaAs, and perovskite-based solar cells.[31–34] From this point of view,

electrically conductive and optically transparent material with a wide bandgap like ZnO is promising as a window layer for $MoTe_2$-based PVSC.[35–37] Here, an initial device structure of Pt/ $MoTe_2/ZnO/ITO/Al$ has been constructed and extensively studied using the SCAPS-1D simulator. The research aims to identify the ideal device conditions for Pt/$MoTe_2/ZnO/ITO/Al$ photovoltaic solar cells (PVSCs). The device's performance has been analyzed via numerical simulations, considering variations in carrier concentration, thickness, and bulk defects of different constituent layers.

One of the major issues is the recombination of minority carriers at the back side, which limits the performance of $MoTe_2$-based SCs.[38] One way to minimize backside recombination and improve the performance is to passivate the backside of the device. In this simulation, N-doped Cu_2O is incorporated into the initial device featuring the configuration of Pt/N-doped $Cu_2O/MoTe_2/ZnO/ITO/Al$ to reduce the recombination of minority carriers and to enhance the collection of photo-generated holes at the back electrode. This is because the N-doped Cu_2O shows high acceptor density and confirms better valence band energy alignment with $MoTe_2$. The key performance parameters of the optimized PVSCs with different back metal work functions, different series and parallel resistances, and different operating temperatures are studied. To understand the potential of the device, the effect of incorporating ZnO as ETL and N-doped Cu_2O as a BSF layer into the proposed device on the built-in potential at different junctions and the recombination rate at different interfaces is also studied. Finally, with an aim to further improve PV performance, one possible approach has been proposed and Pt/N-doped $Cu_2O/$ $MoTe_2/ZnO/ITO/Al$ PVSCs were tested as bifacial PVSCs.

2. Device design and numerical simulation

This study proposes a bi-facial $ZnO/MoTe_2$ device with an N-doped Cu_2O as a BSF layer, aiming to achieve an enhanced V_{OC} through device simulation. This innovative design leverages the unique properties of the selected materials to maximize device performance. The numerical simulations of the proposed Pt/N-doped $Cu_2O/MoTe_2/ZnO/ITO/Al$ PVSCs were performed by using SCAPS-1D software taking 1 sun (100 mW cm^{-2}), AM 1.5 G standard spectrum, and temperature of the device to be 300 K.[39] The step-by-step simulation approach during the SCAPS-1D software operation is presented in Fig. 1. To run the simulation, the scaps3200.exe file is executed, and the entire problem, including all the parameters of the solar cell, is defined. The working point-temperature, frequency, and illumination spectra are specified and remains constant during the entire simulation. The calculation is initiated, and upon completion, the desired data is collected from the specified sections. The SCAPS-1D software mainly solves three pilot equations in semiconductors called the drift–diffusion equation for holes and electrons, Poisson's equation, and free carrier's continuity equations.[40,41] The governing equations are shown below:

Table 1 Lattice parameters of different layers and the percentage of lattice mismatches of their interfaces

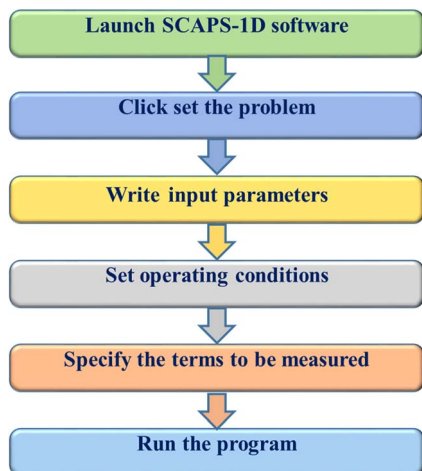| Layer | Lattice parameters | | | Reference | Lattice mismatch (%) |
	a (Å)	b (Å)	c (Å)		
$MoTe_2$	3.53	3.53	13.96	28	
ZnO	3.25	3.25	5.21	29	**8.25** ($ZnO/MoTe_2$)
$N:Cu_2O$	4.29	4.29	4.29	30	**19.43** ($MoTe_2/N:Cu_2O$)

Fig. 1 Schematic of the working approach of the SCAPS-1D simulator.[23]

$$\frac{\partial}{\partial x}\left(\varepsilon_0\varepsilon\frac{\partial\psi}{\partial x}\right) = -q\left(p - n + N_D^+ - N_A^- + \frac{\rho_{def}}{q}\right) \quad (1)$$

$$-\frac{\partial J_n}{\partial x} - U_n + G = \frac{\partial n}{\partial t} \quad (2)$$

$$-\frac{\partial J_p}{\partial x} - U_p + G = \frac{\partial p}{\partial t} \quad (3)$$

$$J_n = -\frac{\mu_n n}{q}\frac{\partial E_{Fn}}{\partial x} \quad (4)$$

$$J_p = +\frac{\mu_p p}{q}\frac{\partial E_{Fp}}{\partial x} \quad (5)$$

ε ascribes the dielectric constant, ψ stands for the electrostatic potential, N_A and N_D are the acceptor and donor density of states, respectively, q is the electrical charge, p is the density of free holes and n is the density of free electrons, J_n is the current density of electrons and J_p is the current density of holes, P_n and P_p define the electron and hole distribution, respectively, E_F denotes the electric field, G is the generation rate, x is the thickness, μ is the carrier mobility, and U represents the rate of recombination.

The first three pilot equations are solved using the Newton–Raphson differentiation methods and Gummel-type iteration to calculate the quasi-Fermi levels and electrostatic potential of free carriers throughout the semiconductor. The electric field, carrier concentration, and other device potential parameters are then determined. Accurate selection of parameters for each layer of the PVSCs is crucial as the accuracy of the performance parameters depends on them. All physical parameters used in this simulation for each layer of the suggested Pt/N-doped Cu$_2$O/MoTe$_2$/ZnO/ITO/Al PVSCs are listed in Table 2. The data derived from the optical properties of MoTe$_2$, ZnO, N-doped Cu$_2$O, and ITO layers are taken from the existing literature for this simulation.[17,42–45]

The device structure, as illustrated in Fig. 2(a), includes zinc oxide (ZnO) as a window layer, N-doped copper oxide (N-doped Cu$_2$O) as a BSF layer, an ITO layer, and aluminum (Al) and platinum (Pt) as the front and back metal electrodes, respectively. The energy band structure of the proposed Pt/N-doped Cu$_2$O/MoTe$_2$/ZnO/ITO/Al PVSCs is portrayed in Fig. 2(b).

3. Results and discussion

3.1 Performance optimization of the MoTe$_2$-based solar cell

3.1.1 Impact of MoTe$_2$ layer on the performance of MoTe$_2$/ZnO PVSC. In Fig. 3, the contour plots illustrate the prime

Table 2 Simulation parameters (baseline) for various constituent layers

Parameters	ITO[46]	ZnO[35]	MoTe$_2$[23]	N-doped Cu$_2$O[17]
Thickness, (μm)	0.050	0.100	1.250	0.100
Band-gap, E_g (eV)	3.60	3.20	1.10	2.60
Electron affinity, χ (eV)	4.50	4.00	4.20	3.20
Dielectric constant, ε_r	8.90	9.00	13.0	6.60
Effective DOS at conduction band density, N_c (cm^{-3})	2.20×10^{18}	4.00×10^{18}	4.00×10^{16}	2.50×10^{20}
Effective DOS at valence band density, N_v (cm^{-3})	1.80×10^{19}	2.00×10^{19}	3.00×10^{18}	2.50×10^{20}
Electron thermal velocity, (cm s^{-1})	1.00×10^7	1.00×10^7	1.00×10^7	1.00×10^7
Hole thermal velocity, (cm s^{-1})	1.00×10^7	1.00×10^7	1.00×10^7	1.00×10^7
Electron carrier mobility, μ_n (cm^2 V^{-1} S^{-1})	50.00	100.0	110.0	0.10
Hole carrier mobility, μ_p (cm^2 V^{-1} S^{-1})	10.00	25.00	426.0	10.00
Donor concentration, N_D (cm^{-3})	1.00×10^{21}	1.00×10^{16}	0.00	0.00
Acceptor concentration, N_A (cm^{-3})	1.00×10^7	0.00	1.00×10^{15}	1.00×10^{19}
Defect density, N_t (cm^{-3})	1.00×10^{14}	1.00×10^{14}	1.00×10^{13}	1.00×10^{15}

Parameters	MoTe$_2$/ZnO		N-doped Cu$_2$O/MoTe$_2$
Types of defect	Neutral		Neutral
Capture cross section of electrons (cm^2)	1.00×10^{19}		1.00×10^{19}
Capture cross section of holes (cm^2)	1.00×10^{19}		1.00×10^{19}
Energetic distribution	0.60		0.60

Fig. 2   Design of the Pt/N-doped Cu$_2$O/MoTe$_2$/ZnO/ITO/Al PVSC (a) schematic blocks and (b) simulated energy band diagram.

operation parameters of the MoTe$_2$/ZnO-based PVSC in relation to the carrier concentration and thickness of the MoTe$_2$ layer. The range for the thickness is from 100 to 2000 nm, and that for the carrier concentration is from 10^{13} to 10^{17} cm^{-3} of the MoTe$_2$ layer. Fig. 3(a) presents that the short-circuit current density (J_{SC}) rises exponentially with increasing thickness up to 1250 nm, beyond which it plateaus. This suggests that enhancing the thickness of the active layer may lead to increased photon absorption, which in turn could generate more electron–hole pairs, and consequently, a higher photo-current.[46] However, beyond a certain thickness, additional photon absorption does not significantly contribute to J_{SC}, as many of the generated carriers may recombine before reaching the electrodes due to increased carrier transit time.[47] It is also observed from Fig. 3(a) that for a MoTe$_2$ absorber layer width of 1500 nm, the maximum value of J_{SC} is 43.5 mA cm^{-2}, which remains relatively steady up to a density of 10^{15} cm^{-3}. Beyond this point, the value of J_{SC} decreases systematically with a further increase in the carrier density of the MoTe$_2$ layer. This is because the recombination losses originating from the coulomb interactions among photo-generated carriers, traps, and defects lead to increased carrier traps and recombination within the absorber layer at elevated carrier doping levels.[48] Conversely, Fig. 3(b) and (c) demonstrate that the V_{OC} and fill factor (FF) show nearly independent characteristics relative to the width of the MoTe$_2$ layer. The V_{OC} is related to J_{SC} and reverse saturation current (J_0) by,

$$V_{OC} \approx \frac{K_B T}{q} \ln \frac{J_{SC}}{J_0} \tag{6}$$

K_B denotes the Boltzmann's constant, q stands for electric charge, and T denotes the absolute temperature.[49] Eqn (6) indicates that the V_{OC} depends not only on the J_{SC} but also on the J_0. As the thickness of the MoTe$_2$ layer increases, both J_{SC} and J_0 increase proportionally, which may balance the J_{SC}/J_0 ratio, leading to an almost constant V_{OC} value.

In Fig. 3(b), it is shown that increasing the doping concentration in a 1500 nm thick MoTe$_2$ layer from 10^{13} cm^{-3} to 10^{17} cm^{-3} results in the V_{OC} rising from 0.4 V to 0.794 V. This rise could be attributed to the shift in the quasi-Fermi energy level of holes as the acceptor concentration (N_A) increases, or due to the heightened potential at the ZnO/MoTe$_2$ junction, which is a consequence of a more robust depletion layer at higher doping densities, thereby improving charge separation and cell efficiency.[17]

In Fig. 3(c), the FF is observed to increase with the MoTe$_2$ layer thickness at 1500 nm and the acceptor level rising from 10^{13} cm^{-3} to 10^{15} cm^{-3}, climbing from 68.39% to 82.33%. This enhancement is linked to the reduced series resistance of the MoTe$_2$ layer as the doping density increases.[50] Nevertheless, a further increment in doping concentration from 10^{15} cm^{-3} to 10^{17} cm^{-3} causes a sharp decline in the FF value from 82.33% to 41.62%, indicating that too high a doping concentration may destabilize the system, leading to a rise in resistance and a fall in FF.

The influence of V_{OC}, J_{SC}, and FF on the PCE of the ZnO/MoTe$_2$ device is depicted in the contour diagram of Fig. 3(d). According to Fig. 3(d), at a doping concentration of 10^{15} cm^{-3}, there is an exponential increase in performance up to a thickness of 1500 nm, after which it plateaus. The observed result stems from the enhancement of photocurrent as the thickness increases; however, recombination may also increase in a thicker absorber layer due to the longer carrier transit time. Furthermore, Fig. 3(d) illustrates that the combined effects of V_{OC}, J_{SC}, and FF enhance the PCE up to a doping density of 10^{15} cm^{-3}, beyond which the PCE begins to decline. The peak PCE of 24.75% was achieved with a MoTe$_2$ layer thickness and doping concentration of 1500 nm and 10^{15} cm^{-3}, respectively.

The defect density within the MoTe$_2$ layer is a critical parameter that significantly impacts the device's performance. Fig. 4 presents contour plots of essential PV parameters against the thickness and defect density of the MoTe$_2$ layer. As shown in
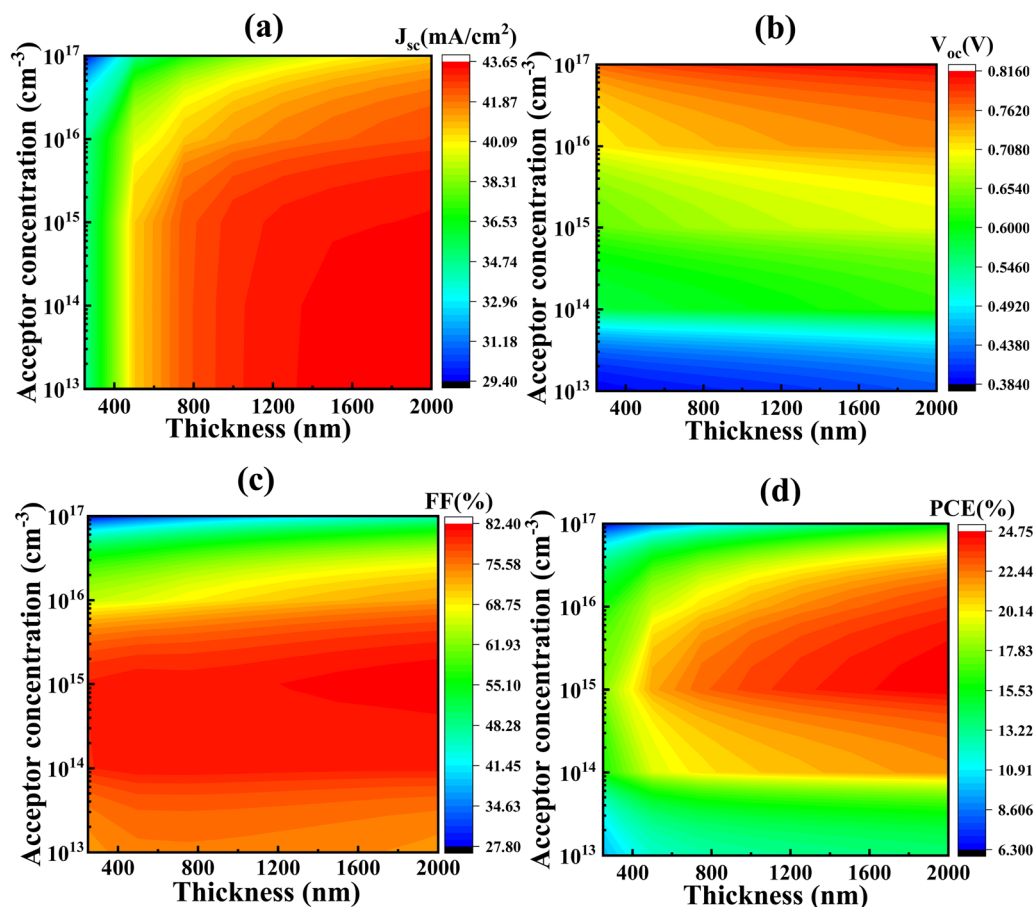
Fig. 3 Contour representations of the variation of (a) J_{SC}, (b) V_{OC}, (c) FF, and (d) PCE depending on the width and doping concentration of the MoTe$_2$ absorber layer. The low to high values of each parameter are indicated by the blue-to-red color coding.

Fig. 4(a), the J_{SC} increases with thickness until a certain defect density of 10^{16} cm^{-3} is reached, beyond which it significantly decreases. Fig. 4(b)–(d) demonstrate that V_{OC} and FF maintain PCE stability with thickness and up to a defect density of 10^{14} cm^{-3}. However, larger defects cause a systematic decline in PCE across all thicknesses. Notably, at a MoTe$_2$ layer thickness of 1500 nm, the V_{OC} drops from 0.69 V to 0.52 V, and the FF decreases from 81.90% to 50.11% as the defect density increases from 10^{14} cm^{-3} to 10^{17} cm^{-3}. This performance degradation results in a substantial efficiency drop, from 24.44% to 2.33%, as the defect density increases from 10^{14} cm^{-3} to 10^{17} cm^{-3}, owing to Shockley–Read–Hall (SRH) recombination and the resulting rise in reverse saturation current.[51,52] Thus, a thickness of 1250 nm, a carrier concentration of 10^{15} cm^{-3}, and a defect density of 10^{14} cm^{-3} are identified as the optimal parameters for the MoTe$_2$ absorber layer for the proposed device structure.

3.1.2 Influence of the ETL layer on the potential of the MoTe$_2$/ZnO-based PVSC. In Fig. 5, the impact of the carrier concentration, thickness, and bulk defect of the ZnO window layer on the performance of the MoTe$_2$/ZnO-based PVSC is illustrated. Fig. 5(a) shows the deviation of the prime performance of the MoTe$_2$/ZnO device with the thickness of the ZnO ETL layer while maintaining the optimized parameters of the

absorber layer from the previous section. The performance parameters, specifically V_{OC}, J_{SC}, FF, and PCE, remain constant at 0.68 V, 43.2 mA cm^{-2}, 82%, and 24%, respectively, across the ZnO layer thickness from 100 nm to 300 nm. The low visible light absorption and wide bandgap of the ZnO electron transport layer are responsible for minimally affecting cell performance.

Fig. 5(b) demonstrates the change in V_{OC}, J_{SC}, FF, and PCE based on the doping concentration of the ZnO window layer, ranging from 10^{13} to 10^{17} cm^{-3}. It is evident from Fig. 5(b) that the donor density does not affect J_{SC}, while a slight decrement in V_{OC} from 0.683 to 0.677 V is observed as the doping density increases. This originates from the coulomb traps due to high donor concentrations, which decrease electron mobility.[53] Moreover, the FF significantly increases from 73 to 84% with the enhanced conductivity of the ZnO window layer due to the increase in doping density.[54] The combined effect of V_{OC}, J_{SC}, and FF leads to an increase in PCE up to a particular doping density of 10^{16} cm^{-3}, which then tends to saturate.

The impact of a rise in defects of the ZnO layer ranging from 10^{12} to 10^{16} cm^{-3} is illustrated in Fig. 5(c). As shown in Fig. 5(c), the performance parameters remain relatively unchanged across this range of defect densities in the ZnO layer. This suggests that the performance of the MoTe$_2$/ZnO-based PVSC is
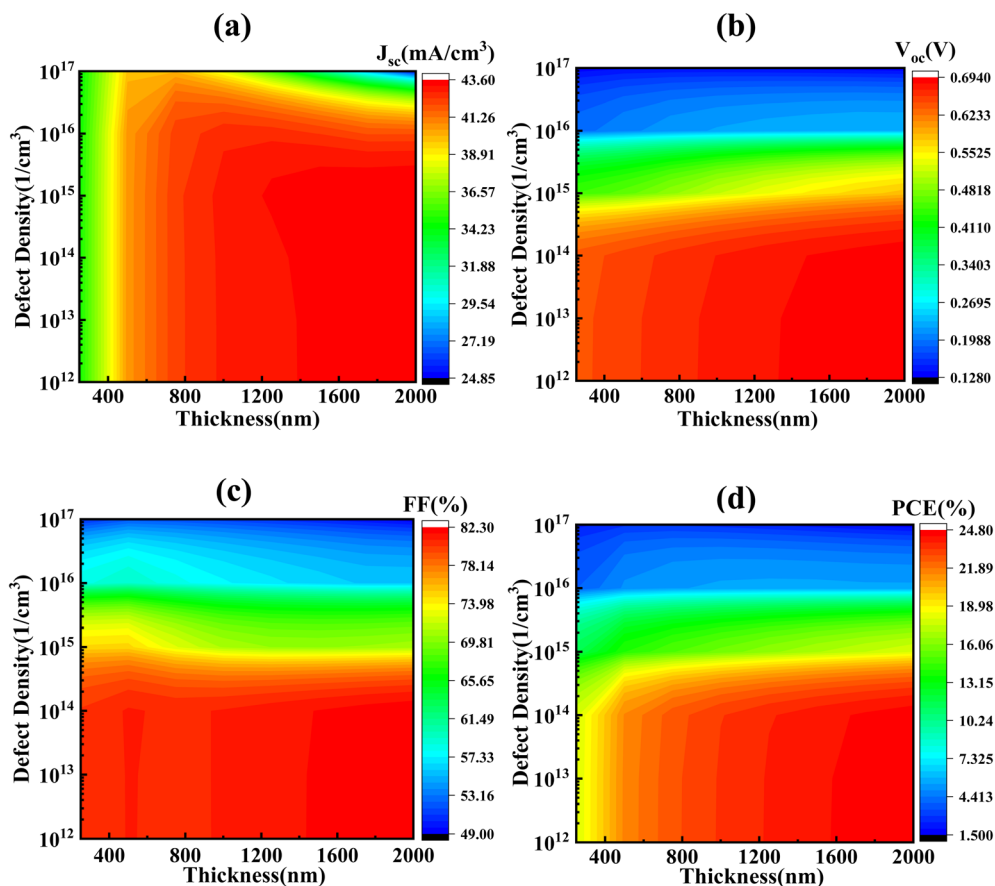
Fig. 4 Contour representations of the variation of (a) J_{SC}, (b) V_{OC}, (c) FF, and (d) PCE of the MoTe$_2$/ZnO device as a function of thickness and defects of the MoTe$_2$ layer. The low to high values of each parameter are indicated by the blue-to-red color coding.
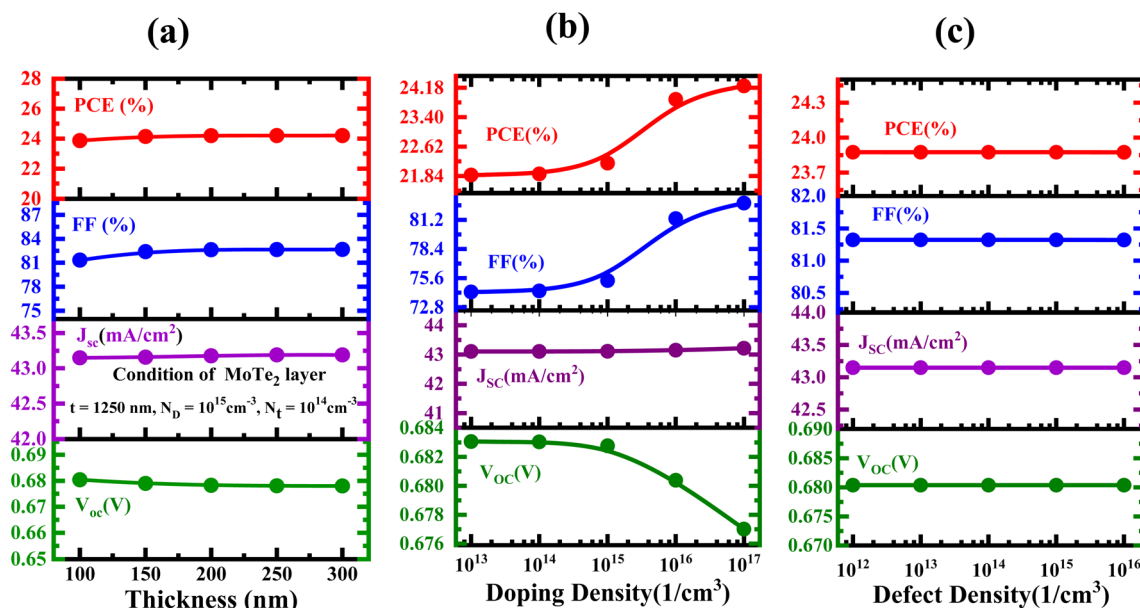

Fig. 5 Variation of MoTe$_2$/ZnO-based PVSC performance on the (a) thickness, (b) donor concentration, and (c) bulk defect density of the ZnO window layer.

not significantly affected by bulk defects in the ZnO layer. Consequently, a ZnO layer with a thickness of 100 nm, carrier concentration of 10^{16} cm^{-3}, and bulk defect density of 10^{14} cm^{-3} is deemed optimal. Conversely, for the MoTe$_2$ layer, a defect density of 10^{13} cm^{-3}, doping concentration of 10^{15} cm^{-3}, and thickness of 1250 nm are identified as the optimal performance conditions for further use.

3.2 MoTe$_2$/ZnO-based PVSC performance dependent on the N-doped Cu$_2$O as a back surface field (BSF) layer

Recombination at the device's rear side significantly hampers the PV performance of solar cells.[17] The Back Surface Field (BSF) layer plays a vital role in solar cell design by enhancing the V_{OC} and overall device performance. This section explores the significance of the BSF layer, detailing its function and impact on solar cell characteristics. The BSF layer's primary role is to minimize electron–hole pair recombination at the back contact, a process that leads to energy loss and reduced efficiency. Typically, the BSF layer is formed by doping the semiconductor material with a specific dopant. In p-type semiconductors like MoTe$_2$, a heavily doped layer acts as the BSF, creating an electric field at the interface that repels minority carriers, leading to a higher V_{OC}.

A BSF with a high carrier density (p^+) is implemented at the back side of the device to reduce surface recombination and enhance performance. N-doped Cu$_2$O is employed as the BSF layer to capitalize on its potential. The energy band structure of the Al/ITO/ZnO/MoTe$_2$/N-doped Cu$_2$O/Pt PVSC under sunlight illumination is depicted in Fig. 2, and the properties of the N-doped Cu$_2$O layer are detailed in Table 2. A minimal conduction band offset (CBO) of approximately 0.06 eV is observed at the conduction band edge between the MoTe$_2$ and ZnO layers, while a significant CBO of about 1.5 eV is present between the absorber and BSF layers. Consequently, electrons generated by

sunlight in the conduction band are reflected by the large CBO at the N-doped Cu$_2$O band edge, facilitating smooth transport across the ZnO/MoTe$_2$ interface due to the small CBO, leading to efficient collection of photo-electrons at the front electrode. Conversely, holes generated in the valence band of the absorber layer are impeded by the ZnO layer and reflected back due to a valence band offset (VBO) of approximately 2.04 eV between ZnO/MoTe$_2$, allowing for their efficient extraction by the N-doped Cu$_2$O layer and transport to the back-electrode, as the VBO between the MoTe$_2$ and N-doped Cu$_2$O layer is insignificantly low.

3.2.1 Dependency of N-doped Cu$_2$O BSF layer on the potential of MoTe$_2$/ZnO-based PVSC.
The effect of the thickness, doping density, and defect density of the N-doped Cu$_2$O BSF layer on the performance of the MoTe$_2$/ZnO-based PVSC is depicted in Fig. 6. Fig. 6(a) displays the variation of key performance of MoTe$_2$/ZnO PVSC in accordance with the thickness of the N-doped Cu$_2$O BSF layer while considering the optimized parameters of the MoTe$_2$-absorber layer and ZnO-window layer from the previous sections. It is observed in Fig. 6(a) that the V_{OC}, J_{SC}, FF, and PCE remain constant at 0.99 V, 43.2 mA cm^{-2}, 79.8%, and 34.45%, respectively, over the N-doped Cu$_2$O BSF layer thickness from 50 nm to 280 nm. This result suggests that no photons from the sunlight were absorbed in the N-doped Cu$_2$O BSF layer.

Fig. 6(b) illustrates the change in key performance parameters of the MoTe$_2$/ZnO PVSC with the carrier density of the N-doped Cu$_2$O BSF layer ranging from 10^{16} cm^{-3} to 10^{21} cm^{-3}. Except for V_{OC}, all the key parameters gradually increased with an increase in the carrier density from 10^{16} cm^{-3} to 10^{18} cm^{-3}, above which the values remained constant in the current density range of 10^{18} cm^{-3} to 10^{21} cm^{-3}. These results suggest that the sufficient electric field due to the BSF layer at the N-
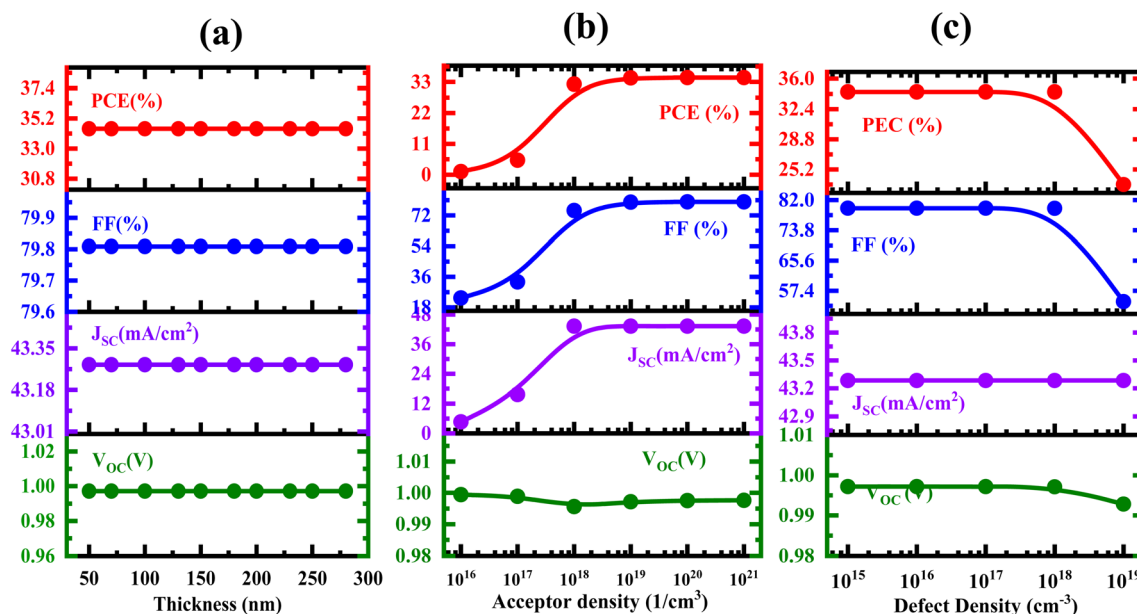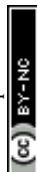

Fig. 6 Dependency of MoTe$_2$/ZnO-based PVSC performance on the (a) thickness, (b) donor concentration, and (c) bulk defect density of the N-doped Cu$_2$O BSF layer.

doped Cu₂O/*MoTe₂* interface might be attained after a certain carrier concentration of 10^{18} cm^{-3}.

The effect of increasing the defect density of the N-doped Cu₂O BSF layer on the key performance parameters is shown in Fig. 6(c). As shown in Fig. 6(c), the performance parameters remain relatively unchanged up to the defect density of 10^{18} cm^{-3} in the N-doped Cu₂O BSF layer. For a large amount of defect density of 10^{19} cm^{-3}, the V_{OC} and FF, resulting in PCE, sharply declined from 34.45% to 23.87% due to Shockley–Read–Hall (SRH) recombination. Consequently, an N-doped Cu₂O BSF layer with a thickness of 100 nm, carrier concentration of 10^{19} cm^{-3}, and bulk defect density of 10^{15} cm^{-3} is considered optimal.

3.2.2 Impact of the BSF layer on the built-in potential of the device. In Fig. 7, the capacitance–voltage (C–V) characteristics are presented using Mott–Schottky analysis to find the built-in potential (φ_{bi}) for two device configurations: one without a BSF layer (ZnO/MoTe₂) and the other with a BSF layer (N-doped Cu₂O/MoTe₂/ZnO). The built-in potential (φ_{bi}) can be estimated from the intercept of the $(1/C)^2$–V plot.[55–59]

$$\frac{1}{C^2} = \frac{c\left(\frac{KT}{q} - \varphi_{bi} - V\right)}{qA^2\varepsilon_0\varepsilon_{CTS}N_D} \tag{7}$$

ε_{CTS} and ε_0 represent the permittivity of the medium and vacuum, respectively, C is the resultant capacitance at the junctions, V defines the applied voltage, N_D demonstrates the donor density, $q = 1.6 \times 10^{19}$ eV, and A describes the area of the diode.

The linear section in Fig. 7(a), after fitting and extrapolation, reveals that the built-in potential (φ_{bi}) for the ZnO/MoTe₂ device is approximately 0.72 V. However, the built-in potential for the ZnO/MoTe₂/N-doped Cu₂O device is determined to be 1.18 V. It is suggested that the cumulative effect of the ZnO/MoTe₂ junction and MoTe₂/N-doped Cu₂O interface is responsible for improving the device's built-in potential, thereby aiding in the efficient separation of photo-induced carriers. The enhanced electric field created by the BSF layer promotes the drift of

minority carriers towards the front contact, where they can contribute to the photocurrent. This results in a slightly improved J_{SC} in the device. Additionally, due to the higher CB edge of the N-doped Cu₂O compared to the MoTe₂ edge, electrons generated in the absorber layer are repelled at the BSF layer's CB edge. This repulsion mitigates surface recombination at the rare interface, leading to a significantly higher V_{OC} of the ZnO/MoTe₂/N-doped Cu₂O device. In other words, introducing a properly designed Back Surface Field (BSF) layer on the backside of the device generates an additional electric field at the BSF/Absorber (p^+/p) interface.[60] This electric field causes the reflection of minority carriers (electrons) approaching the BSF/Absorber (p^+/p) interface. As a result, the recombination velocity, which refers to the number of carrier recombination per unit area and time, will decrease due to the presence of the electric field produced by the BSF layer. This reduction in recombination leads to an improvement in the open-circuit voltage (V_{OC}) of the device.

3.2.3 Impact of N-doped Cu₂O BSF layer on the Recombination rate at different regions of the device. Shockley–Read–Hall (SRH) recombination, known as defect-assisted recombination, is a key process in solar cells and can significantly reduce cell performance. Statistical analysis and analytical approximations of SRH recombination are crucial for understanding and quantifying recombination rates (R) in different regions of the solar cell, such as in the bulk region (R^b), depletion region (R^d), at the ETL/absorber interface ($R^{i,f}$), and the BSF layer/absorber interface ($R^{i,b}$).[61] Our previous article details the methodology for estimating these recombination rates at different regions of the device.[62] The V_{OC} is related to the intensity of the light as follows:

$$V_{OC} = \frac{2K_BT}{q}\ln\left[K_1\left(\sqrt{(G_aK_2 + 1)} - 1\right)\right] \tag{8}$$

Here, K_B represents the Boltzmann constant, q is the electron charge, G_a is the incident light intensity, and T is the absolute temperature. Coefficients K_1 and K_2 are derived from fitting the intensity-dependent V_{OC} curves using eqn (8).
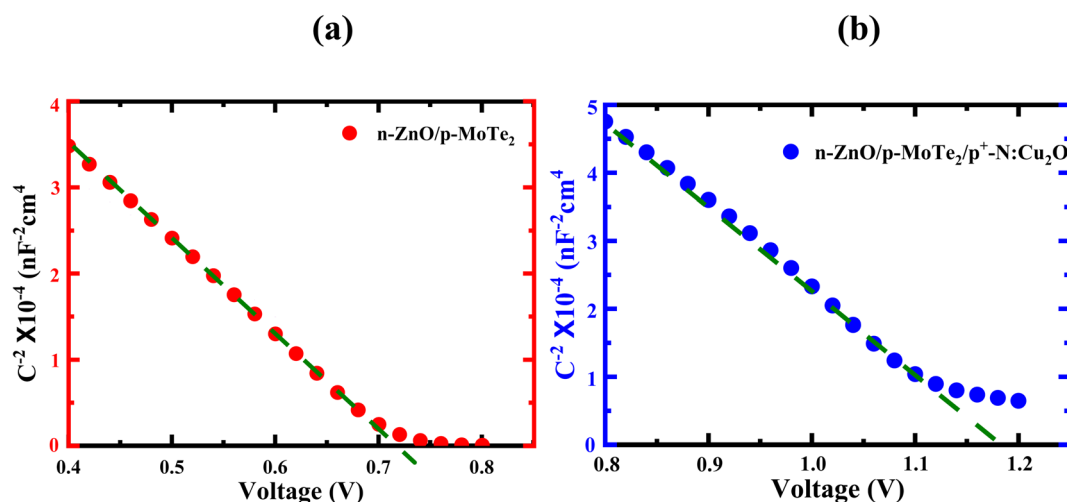

(a)   **(b)**

Fig. 7 C–V analysis to evaluate the built-in potential of (a) ZnO/MoTe₂ and (b) ZnO/MoTe₂/N-doped Cu₂O heterostructures.
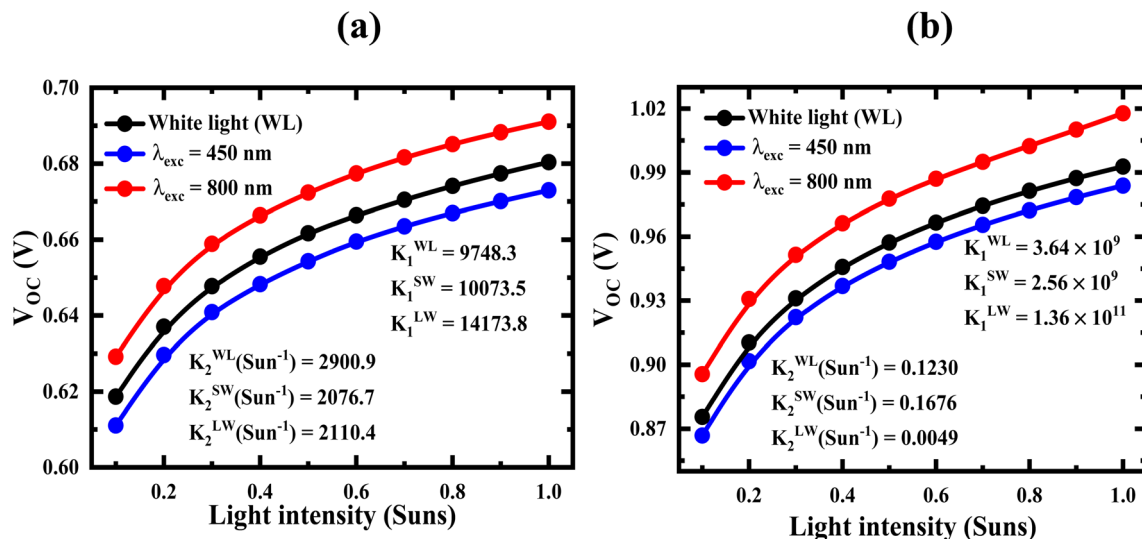
Fig. 8 Light intensity-dependent V_{OC} for (a) ZnO/MoTe$_2$ (b) ZnO/MoTe$_2$/N-doped Cu$_2$O device with different excitation wavelengths of white light (WL), λ_{exc} = 450 nm, and λ_{exc} = 800 nm at a constant temperature of 300 K.

An intensity-dependent V_{OC} analysis under monochromatic short and long wavelengths has been conducted to extract the recombination coefficient at the absorber/BSF interface ($R_0^{i,b}$) and the surface recombination velocity (SRV) of electrons at the absorber/BSF interface. The study uses two monochromatic wavelengths, 450 nm and 800 nm, to illuminate the designed SCs for qualitative and quantitative assessments of recombination at the back interface without and with the BSF layer. Fig. 8 shows the V_{OC} graphs dependent on light intensity (G_a) without and with the BSF layer. The K_1 and K_2 values, obtained from fitting the intensity-dependent V_{OC} curves in Fig. 8 using eqn (8), are used to calculate the recombination coefficients R_0^d, $R_0^{i,b}$, and hence recombination rates R^d, $R^{i,b}$ as well as the surface recombination velocity of electrons at the back interface, which are presented in Table 3. Details of calculations of the recombination coefficient and surface recombination velocity are discussed in ES1.†

Table 3 reveals that the recombination coefficient and rate in the depletion region and at the back interface, along with the SRV at the back interface for ZnO/MoTe$_2$, are notably poor. However, by integrating an N-doped Cu$_2$O layer (100 nm) with ZnO/MoTe$_2$, forming a ZnO/MoTe$_2$/N-doped Cu$_2$O structure, a significant reduction in the recombination coefficient in the depletion region and at the back interface, from 1.1×10^8 cm^{-2} s^{-1} to 7.1×10^6 cm^{-2} s^{-1} and 1.6×10^3 cm^{-2} s^{-1} to 1.3×10^{-3}, respectively, is observed. Consequently, the recombination rate in the depletion region and at the back interface is suppressed from 2.77×10^{16}

cm^{-2} s^{-1} to 1.75×10^{15} and 3.98×10^{11} cm^{-2} s^{-1} to 3.35×10^5, respectively. Additionally, the SRV at the back interface is decreased from 200 cm s^{-1} to 1.69×10^{-3} cm s^{-1} by adding the N-doped Cu$_2$O BSF layer. These findings imply that the electric field at the MoTe$_2$/N-doped Cu$_2$O interface enhances hole transport at the valence band from the MoTe$_2$ absorber layer to the back contact *via* the N-doped Cu$_2$O-BSF layer, mitigating the flow of minority carriers (electrons) towards the MoTe$_2$/N-doped Cu$_2$O junction at the conduction band, thus reducing the carrier recombination rate at the device's rear side, suppressing the dark current (J_0). It is confirmed from eqn (6) that the open circuit voltage of the MoTe$_2$-based PVSC in the presence of N-doped Cu$_2$O is improved due to the suppression of the dark current.

3.2.4 Impact of BSF layer on the open-circuit voltage (V_{OC}) of the device. Fig. 9 compares the performance of the MoTe$_2$/ZnO-based PVSC with and without the N-doped Cu$_2$O BSF layer. The J-V characteristics of both ZnO/MoTe$_2$ and ZnO/MoTe$_2$/N-doped Cu$_2$O PVSCs are displayed in Fig. 9(a), where the key performance parameters are also detailed. The ZnO/MoTe$_2$ single-junction SC shows an efficiency of 23.87%, with a J_{SC} of 43.15 mA cm^{-2}, V_{OC} of 0.68 V, and FF of 81.31%. Incorporating a 100 nm thick N-doped Cu$_2$O as the BSF layer into the ZnO/MoTe$_2$ SC significantly enhances the efficiency to 34.45%, with a J_{SC} of 43.28 mA cm^{-2}, V_{OC} of 1.0 V, and an FF of 79.81%. The notable increase in efficiency is primarily due to the raised V_{OC} (from 0.68 V to 1.0 V), which is a result of a stronger built-in

Table 3 Extracted values of K_1 and K_2 from Fig. 8 and recombination coefficient for MoTe$_2$-based PVSCs with and without N-doped Cu$_2$O BSF layer. Here, R_0^d, $R_0^{i,b}$, R^d, $R^{i,b}$, and S_e^b are calculated at a bias voltage of 1.0 V

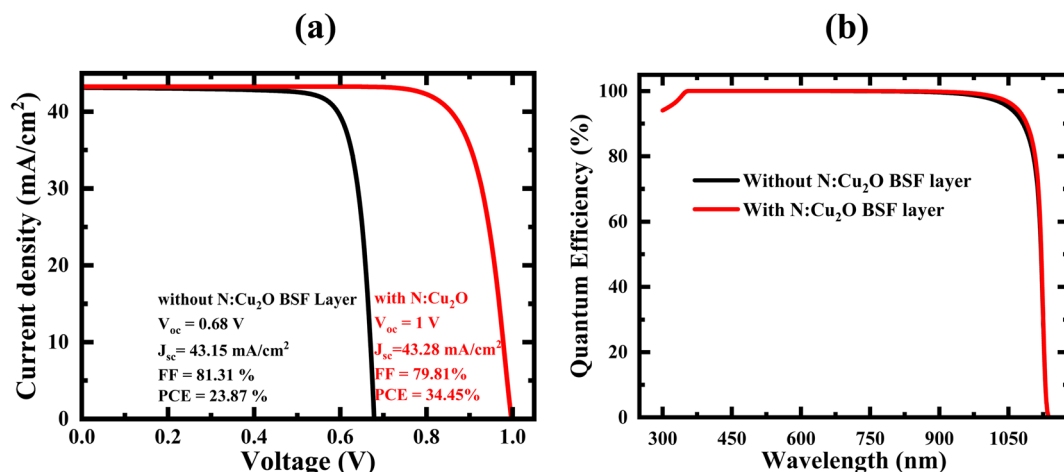| Condition	K_1^{SW}	K_1^{LW}	K_1^{WL}	K_2^{SW}	K_2^{LW}	K_2^{WL}	R_0^d (cm^{-2} s^{-1})	$R_0^{i,b}$ (cm^{-2} s^{-1})	R^d (cm^{-2} s^{-1})	$R^{i,b}$ (cm^{-2} s^{-1})	S_e^b (cm s^{-1})
Without N-doped Cu$_2$O-BSF layer	10 073	14 173.8	9748.3	2076.7	2110.4	2901	1.1×10^8	1.6×10^3	2.77×10^{16}	3.98×10^{11}	200
with N-doped Cu$_2$O-BSF layer	2.56×10^9	1.36×10^{11}	3.64×10^9	0.1676	0.0049	0.123	7.1×10^6	1.3×10^{-3}	1.75×10^{15}	3.35×10^5	1.69×10^{-3}

Fig. 9 (a) Light-dependent output characteristic and (b) quantum efficiency curves for the proposed $MoTe_2$/ZnO PVSC in the presence and absence of an N-doped Cu_2O-BSF layer.

potential (from 0.72 eV to 1.18 eV) in the $ZnO/MoTe_2$/N-doped Cu_2O heterostructure, thus reducing recombination losses.

Fig. 9(b) compares the quantum efficiency (QE) curves for both structures in the presence and absence of the N-doped Cu_2O BSF layer. Simulations spanning a wavelength range of 300 nm to 1200 nm under AM1.5 solar illumination indicate similar QE curves for both cases. It is evident that the $MoTe_2$/ZnO PVSC, in the presence and absence of the N-doped Cu_2O BSF layer, exhibits nearly identical QE curves, indicating the N-doped Cu_2O BSF layer does not contribute to photon absorption. However, it aids in enhancing the built-in potential by the additional N-doped $Cu_2O/MoTe_2$ junction, reducing recombination losses at the back side of the device to increase the V_{OC}, leading to improved photovoltaic efficiency (Fig. 8).

3.3　Effect of metal work function at the back contact and operation temperature on the N-doped $Cu_2O/MoTe_2$/ZnO PVSC

In Fig. 10(a), the graph shows the normalized PV response for the back-contact metal work function ranging from 5.1 eV to 5.7 eV. This is to understand the behavior at the interface of the back-contact/BSF layer, whether it is ohmic or rectifying. The carrier concentration, thickness, and bulk defect of each layer have been kept at the optimized values obtained previously from the simulation. From Fig. 10(a), it can be observed that all the PV parameters except for J_{SC} linearly increase with the increasing anode's work function up to a certain value of 5.32 eV. Beyond this value, further improvement in the metal work function of the back electrode shows diminishing returns. It is also noted in Fig. 10(a) that a Schottky-type rectifying behavior is observed at the N-doped Cu_2O/anode interface for work functions less than 5.32 eV. This leads to the recombination of carriers at the back-contact/BSF interface, resulting in reduced V_{OC}, FF, and consequently, photovoltaic efficiency, as shown in Fig. 10(a). It is well known that the energy barrier (φ_B) between the back surface anode metal and N-doped Cu_2O-BSF layer can be evaluated by:

$$\varphi_B = \frac{E_g}{q} + \mathcal{X} + \varphi_m \qquad (9)$$
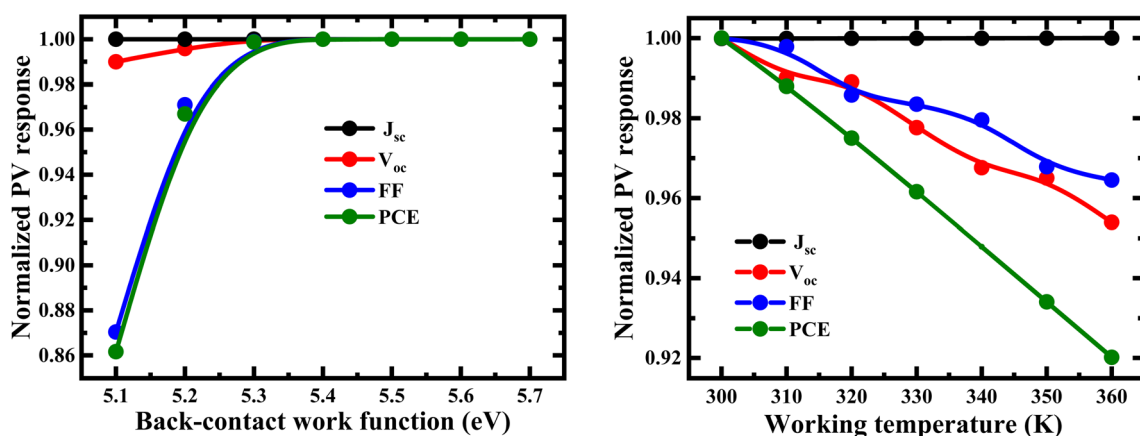

Fig. 10 Key performance parameter responses of the N-doped Cu2O/MoTe2/ZnO PVSC in relation to (a) work function of the back-contact metal and (b) operating temperature.

Here, χ defines the electron affinity of N-doped Cu_2O (3.20 eV), E_g ascribes the bandgap of N-doped Cu_2O (2.60 eV), and φ_m denotes the work function of the anode metal. According to eqn (9), for the anode metals with work function 5.32 eV, the energy barrier is about 0.48 eV; such a small value may not affect the V_{OC} and FF of the device.[62,63] Thereby, the maximum PVSC performance might be achieved for the anode with a metal work function of more than 5.32 eV. This finding suggests that a relatively high work function anode materials (>5.32 eV), such as Pt (5.65 eV),[64] Au(111) (5.37 eV),[65] Ni(111) (5.35 eV)[66] and Pd(111) (5.40 eV),[65] are required to establish the maximum efficiency of the N-doped Cu_2O/$MoTe_2$/ZnO PVSC.

Conventionally, solar cells are typically designed to operate within a temperature range of 288 to 323 K when placed in the open air.[67] The operating temperature is a critical factor as it greatly affects the PV response of the cells.[68] Fig. 10(b) displays the effect of operating temperature on the optimized N-doped Cu_2O/$MoTe_2$/ZnO PVSC. It is noticed from Fig. 10(b) that a linear decrement of the V_{OC} and FF leads to a decrease in PCE as the working temperature increases. This observation suggests that at higher temperatures, electrons acquire sufficient energy to recombine with holes before leaving the depletion zone.[69] The temperature coefficient C_T (% K^{-1}) of PCE is a key parameter for PV devices to assess their stability, indicating how elevated operating temperatures impact the device's PCE, and can be expressed under standard test conditions (STC: 298 K) as follows:[60]

$$C_T = \frac{1}{\eta_{STC}} \frac{d\eta_T}{dT} \times 100\% \qquad (10)$$

η_{STC} ascribes the cell efficiency at standard test conditions (STC: 298 K) and $\frac{d\eta_T}{dT}$ is extracted from the slope by fitting the PCE curve in Fig. 10(b). Now, using eqn (10), the temperature coefficient of PCE of the cell is evaluated to be -0.133% K^{-1}, which is less than that of traditional Si (-0.5% K^{-1}) and CIGS (-0.443% K^{-1}) solar cells.[23,70]

3.4 Bifacial nature of the ZnO/$MoTe_2$/N-doped Cu_2O solar cell

The bifacial device is a strong candidate for improving energy harvesting capabilities per unit area to replace mono-facial solar cells without increasing cost and manufacturing complexity. Two independent simulations for back and front side illuminations of 1 sun are considered. The term bifacial factor (BF) is carried out to understand the asymmetric photoelectric behavior of bifacial devices. The relative feedback of each side can be realized by the BF, which is estimated by the following equation.

$$BF = \frac{X_{back}}{X_{front}} \qquad (11)$$

X defines any PV parameter (V_{OC}, J_{SC}, FF or PCE) of the device under the back and front illumination at 1 sun.

Fig. 11 shows the J–V curves of an optimized N-doped Cu_2O/$MoTe_2$/ZnO solar cell under both front and back illumination at
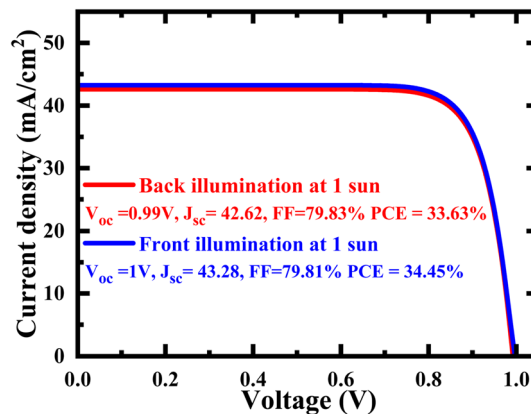

Fig. 11 J–V curves of the optimized N-doped Cu_2O/$MoTe_2$/ZnO PVSC under back-illumination at 1 sun and front illumination at 1 sun for a bifacial PVSC.

1 sun. The PV performance slightly declines with back illumination at 1 sun, suggesting minor absorption losses at the device's rear surface. The bifacial factor (BF) for V_{OC} and FF is calculated to be 99.49% and 99.89%, respectively, indicating negligible additional losses impacting V_{OC} and FF under backside illumination. The BF for J_{SC} is approximately 98.4%, reflecting a slight reduction in J_{SC} due to absorption losses at the solar cell's back surface. Lastly, a BF for PCE of 97.6% is reported, corroborating earlier studies.[17,71]

4. Conclusion and recommendations

Despite the inherent advantages of $MoTe_2$, developing high-efficiency $MoTe_2$-based solar cells faces a crucial challenge: achieving a high open-circuit voltage (V_{OC}). The V_{OC} is a key performance parameter that directly influences the overall efficiency of a solar cell. A high V_{OC} is essential for maximizing the power output and achieving competitive efficiencies. This study examines the obstacles related to attaining a high V_{OC} in $MoTe_2$ thin film solar cells. It examines the pivotal role of the Back Surface Field (BSF) layer in enhancing V_{OC} and introduces a novel bi-facial ZnO/$MoTe_2$ solar cell with an N-doped Cu_2O BSF layer. Our methodology relies on extensive device simulations utilizing the SCAPS-1D software to offer insights into the electrical properties and performance of the proposed device architecture. This study numerically investigated the potential of a bi-facial ZnO/$MoTe_2$ solar cell with an N-doped Cu_2O BSF layer for achieving high V_{OC}. The incorporation of the N-doped Cu_2O BSF layer effectively suppressed carrier recombination at the back contact, leading to a significant enhancement in V_{OC}. The proposed device structure demonstrated a considerable increase in V_{OC} compared to conventional designs, potentially enabling higher power conversion efficiency. The simulation results highlighted the importance of optimizing the thickness and doping concentration of the BSF layer to maximize its effectiveness. This research provides valuable insights into the design and optimization of $MoTe_2$-based solar cells. Future research efforts should focus on:

Experimental validation: conducting experimental fabrication and characterization of the proposed device structure to validate the simulation results.

Optimization of BSF layer: investigating different materials and deposition techniques for the BSF layer to further enhance its performance.

Integration with other technologies: exploring the integration of the bi-facial design with other advanced technologies, such as tandem solar cells or flexible substrates.

By addressing these recommendations, the development of high-performance $MoTe_2$ solar cells with improved J_{SC} and power conversion efficiency can be significantly accelerated, contributing to the advancement of renewable energy technologies.

Data availability

The data that support the findings of this study are available from the corresponding authors upon reasonable request.

Conflicts of interest

The authors declare that there is no conflicts of interest in this work.

Acknowledgements

References

1 M. T. Rizi, M. H. S. Abadi and M. Ghaneii, Two dimensional modeling of Cu_2O heterojunction solar cells based-on β-Ga_2O_3 buffer, *Optik*, 2018, **155**, 121–132.

2 Z. Shi and A. H. Jayatissa, One-pot hydrothermal synthesis and fabrication of kesterite $Cu_2ZnSn(S,Se)_4$ thin films, *Prog. Nat. Sci.:Mater. Int.*, 2017, **27**, 550–555.

3 S. A. Vanalakar, P. S. Patil and J. H. Kim, Recent advances in synthesis of Cu_2FeSnS_4 materials for solar cell applications: a review, *Sol. Energy Mater. Sol. Cells*, 2018, **182**, 204–219.

4 J. Li, D. Wang, X. Li, Y. Zeng and Y. Zhang, Cation substitution in earth-abundant kesterite photovoltaic materials, *Adv. Sci.*, 2018, **5**, 1700744.

5 O. A. M. Abdelrauf and N. K. Allam, Nanostructuring for enhanced absorption and carrier collection in CZTS-based solar cells: coupled optical and electrical modeling, *Opt. Mater.*, 2016, **54**, 84–88.

6 R. W. Fessenden, J. Sobhanadri and V. Subramanian, Minority carrier lifetime in thin films of Zn,P, using microwave and optical transient measurements, *Thin Solid Films*, 1995, **266**, 176–181.

7 G. Sai Gautam, T. P. Senftle and E. A. Carter, Understanding the effects of Cd and Ag doping in Cu_2ZnSnS$_4$ solar cells, *Chem. Mater.*, 2018, **30**, 4543–4555.

8 K. Branker, M. J. M. Pathak and J. M. Pearce, A review of solar photovoltaic levelized cost of electricity, *Renewable Sustainable Energy Rev.*, 2011, **15**, 4470–4482.

9 W. Ma, J. M. Luther, H. Zheng, Y. Wu and A. P. Alivisatos, Photovoltaic Devices Employing Ternary PbS_xSe_{1-x} Nanocrystals, *Nano Lett.*, 2009, **9**, 1699–1703.

10 W. Ma, S. L. Swisher, T. Ewers, J. Engel, V. E. Ferry, H. A. Atwater and A. P. Alivisatos, Photovoltaic Performance of Ultrasmall PbSe Quantum Dots, *ACS Nano*, 2011, **5**, 8140–8147.

11 S. McDonald, G. Konstantatos, S. Zhang, P. Cyr, E. Klem, L. Levina and E. Sargent, Solution-Processed PbS Quantum Dot Infrared Photodetectors and Photovoltaics, *Nat. Mater.*, 2005, **4**, 138–144.

12 Z. Ning, D. Zhitomirsky, V. Adinolfi, B. Sutherland, J. Xu, O. Voznyy, P. Maraghechi, X. Lan, S. Hoogland, Y. Ren and E. H. Sargent, Graded Doping for Enhanced Colloidal Quantum Dot Photovoltaics, *Adv. Mater.*, 2013, **25**, 1719–1723.

13 W. Zhao, R. M. Ribeiro, M. Toh, A. Carvalho, C. Kloc, A. H. C. Neto and G. Eda, Origin of Indirect Optical Transitions in Few-Layer MoS_2, WS_2, and WSe_2, *Nano Lett.*, 2013, **13**, 5627–5634.

14 S. Dominguez-Meister, A. Justo and J. Sanchez-Lopez, Synthesis and tribological properties of WSe_x films prepared by magnetron sputtering, *Mater. Chem. Phys.*, 2013, **142**, 186–194.

15 C. Chiritescu, D. G. Cahill, N. Nguyen, D. Johnson, A. Bodapati, P. Keblinski and P. Zschack, Ultralow Thermal Conductivity in Disordered, Layered WSe_2 Crystals, *Science*, 2007, **315**, 351–353.

16 S. T. Finn and J. E. Macdonald, Contact and Support Considerations in the Hydrogen Evolution Reaction Activity of Petaled MoS_2 Electrodes, *ACS Appl. Mater. Interfaces*, 2016, **8**, 25185–25192.

17 M. A. Rahman, Performance analysis of WSe_2-based bifacial solar cells with different electron transport and hole transport materials by SCAPS-1D, *Heliyon*, 2022, **8**, e09800.

18 J. Liu, Y. Wang, X. Xiao, K. Zhang, N. Guo, Y. Jia, S. Zhou, Y. Wu, Q. Li and L. Xiao, Conversion of Multi-layered $MoTe_2$ Transistor Between P-Type and N-Type and Their Use in Inverter, *Nanoscale Res. Lett.*, 2018, **13**(291), 1–9.

19 N. Rahman, M. D. Haque, M. F. Rahman, M. M. Islam, M. A. N. Juthi, A. R. Roy, M. A. Akter and M. F. Islam, Assessing the performance of $MoTe_2$ based solar cell with Cu_2O hole transport layer through device simulation, *Discover Mater.*, 2023, **3**(25), 1–7.

20 C. Gong, H. Li, H. Wang, C. Zhang, Q. Zhuang, A. Wang, Z. Xu, W. Cai, R. Li, X. Li and Z. Zang, Silver coordination-induced n-doping of PCBM for stable and efficient inverted perovskite solar cells, *Nat. Commun.*, 2024, **15**, 4922.

21 K. Wang, Z. Xu, Z. Guo, H. Wang, S. M. H. Qaid, K. Yang and Z. Zang, Phosphonate Diacid Molecule Induced Crystallization Manipulation and Defect Passivation for High-Performance Inverted MA-Free Perovskite Solar Cells, *Adv. Energy Mater.*, 2024, **14**, 2402249.

22 C. Zhang, H. Li, C. Gong, Q. Zhuang, J. Chen and Z. Zang, Crystallization manipulation and holistic defect passivation toward stable and efficient inverted perovskite solar cells, *Energy Environ. Sci.*, 2023, **16**, 3825–3836.

23 A. Rajib, M. A. A. Kafi, M. M. H. Najesh, M. R. Hasan, M. R. Miah and A. Rahman, Performance analysis of 2D-MoTe$_2$/2D-MoSe$_2$-based bifacial solar cells with N-doped Cu$_2$O as BSF Layer by SCAPS-1D, *Phys. Scr.*, 2024, **99**, 055541.

24 A. Rajib, A. Kuddus, K. Yokoyama, T. Shida, K. Ueno and H. Shirai, Mist chemical vapor deposition of Al$_{1-x}$Ti$_x$O$_y$ thin films and their application to a high dielectric material, *J. Appl. Phys.*, 2022, **131**, 105301.

25 A. Rajib, A. Kuddus, T. Shida, K. Ueno and H. Shirai, Mist Chemical Vapor Deposition of AlO$_x$ Thin Films Monitored by a Scanning Mobility Particle Analyzer and its Application to the Gate Insulating Layer of Field-effect Transistors, *ACS Appl. Electron. Mater.*, 2021, **3**(2), 658–667.

26 A. Kuddus, A. Rajib, K. Yokoyama, T. Shida, K. Ueno and H. Shirai, Mist Chemical Vapor Deposition of Crystalline MoS$_2$ Atomic Layer Films for Field-Effect Transistors, *Nanotechnology*, 2021, **33**(4), 045601.

27 B. Sultana, A. T. M. Islam, Md. Haque, A. Kuddus, Md. Ali and F. Rahman, Numerical study of MoSe$_2$-based dual-heterojunction with In$_2$Te$_3$ BSF layer toward high-efficiency photovoltaics, *Phys. Scr.*, 2023, **98**, 095935.

28 D. Puotinen and R. E. Newnham, The crystal structure of MoTe$_2$, *Acta Crystallogr.*, 1961, **14**, 691–692.

29 R. R. Reeber, Lattice parameters of ZnO from 4.2^0 to 296 ^{0}K, *J. Appl. Phys.*, 1970, **41**, 5063–5066.

30 Y. Wang, J. Ghanbaja, D. Horwat, L. Yu and J. F. Pierson, Nitrogen chemical state in N-doped Cu$_2$O thin films, *Appl. Phys. Lett.*, 2017, **110**, 131902.

31 I. Alam, R. Mollick and Md. A. Ashraf, Numerical simulation of Cs$_2$AgBiBr$_6$-based perovskite solar cell with ZnO nanorod and P3HT as the charge transport layers, *Phys. B*, 2021, **618**, 413187.

32 S. S. A. Askari, M. Kumar and M. K. Das, Numerical study on the interface properties of a ZnO/c-Si heterojunction solar cell, *Semicond. Sci. Technol.*, 2018, **33**, 115003.

33 N. Dinh Lam, Modelling and numerical analysis of ZnO/CuO/Cu$_2$O heterojunction solar cell using SCAPS, *Eng. Res. Express*, 2020, **2**, 025033.

34 M. Manoua, T. Jannane, K. El-Hami and L. Ahmed, Investigation of *n*-ZnO/*p*-GaAs Heterojunction Solar Cell Using Two-Dimensional Numerical Simulation, *Recent Adv. Photonics Optoelectron.*, 2023, **75**, 3601–3611.

35 B. Mozafari and A. Shahhoseini, Using Molybdenum Trioxide as a TCO Layer to Improve Performance of CdTe/CdS1 Thin-film Solar Cell, *Signal Process. Renew. Energy*, 2020, **4**(3), 57–65.

36 D. Parajuli, K. C. Devendra, K. B. Khattri, D. R. Adhikari, R. A. Gaib and D. K. Shah, Numerical assessment of optoelectrical properties of ZnSe–CdSe solar cell-based with ZnO antireflection coating layer, *Sci. Rep.*, 2023, **13**, 12193.

37 Y. A. Wahmane, H. Mouhib, B. Ydir, A. A. Hssi, L. Atourki, A. Ihlal and K. Bouabid, Comparison study between ZnO and TiO$_2$ in CuO based solar cell using SCAPS-1D, *Mater. Today Proc.*, 2022, **52**, 166–171.

38 M. Gholipoor, N. Solhtalab and M. H. Mohammadi, High-performance parallel tandem MoTe$_2$/perovskite solar cell based on reduced graphene oxide as hole transport layer, *Sci. Rep.*, 2022, **12**, 20455.

39 I. Kriegel, J. Rodriguez-Fernandez, E. Da Como, A. A. Lutich, J. M. Szeifert and J. Feldmann, Tuning the Light Absorption of Cu1.97S Nanocrystals in Supercrystal Structures, *Chem. Mater.*, 2011, **23**, 1830–1834.

40 M. Burgelman, J. Verschraegen, S. Degrave and P. Nollet, Modeling thin-film PV devices, *Prog. Photovoltaics*, 2004, **12**(2–3), 143–153.

41 M. Burgelman, P. Nollet and S. Degrave, Modelling polycrystalline semiconductor solar cells, *Thin Solid Films*, 2000, **361**, 527–532.

42 F. Liu, J. Zhu, J. Wei, Y. Li, M. Lv, S. Yang, B. Zhang, J. Yao and S. Dai, Numerical simulation: Toward the design of high-efficiency planar perovskite solar cells, *Appl. Phys. Lett.*, 2014, **104**, 253508.

43 K. Wu, H. Ma, Y. Gao and J. Yang, Highly-efficient heterojunction solar cells based on two-dimensional tellurene and transition metal dichalcogenides, *J. Mater. Chem. A*, 2019, **7**, 7430–7436.

44 B. K. Mondal, S. K. Mostaque and J. Hossain, Unraveling the effects of a GeSe BSF layer on the performance of a CuInSe$_2$ TFSCs: a computational analysis, *Opt. Continuum*, 2023, **2**, 428–440.

45 A. Bedia, F. Z. Bedia, M. Aillerie and B. Benyoucef, Morphological and Optical Properties of ZnO Thin Films Prepared by Spray Pyrolysis on Glass Substrates at Various Temperatures for Integration in Solar Cell, *Energy Procedia*, 2015, **74**, 529–538.

46 J. Hossain, M. Rahman, M. M. A. Moon, B. K. Mondal, M. F. Rahman and M. H. K. Rubel, Guidelines for a highly efficient CuI/n-Si heterojunction solar cell, *Eng. Res. Express*, 2020, **2**, 045019.

47 S. M. Sze and K. K. Ng, LEDs and lasers, *Phys. Semicond. Devices*, 2006, **3**, 601–657.

48 M. D. Wanda, S. Ouédraogo, F. Tchoff, F. Zougmoré and J. M. B. Ndjaka, Numerical Investigations and Analysis of Cu$_2$ZnSnS$_4$ Based Solar Cells by SCAPS-1D, *Int. J. Photoenergy*, 2016, 1–9.

49 B. H. Patel and S. S. Patel, Growth and electrical properties of flash evaporated AgGaTe$_2$ thin films, *Cryst. Res. Technol.*, 2006, **41**(2), 117–122.

50 A. Rana, A. Kumar, M. W. Rahman, N. Vashistha, K. K. Garg, S. Pandey and R. K. Singh, Non-approximated series resistance evaluation by considering high ideality factor in organic solar cell, *AIP Adv.*, 2018, **8**, 125121.

51 N. F. Mott, Metal-insulator transition, *Rev. Mod. Phys.*, 1968, **40**(4), 677.

52 S. Rai, B. K. Pandey and D. K. Dwivedi, Modeling of highly efficient and low cost CH$_3$NH$_3$Pb (I$_{1-x}$Cl$_x$)$_3$ based perovskite solar cell by numerical simulation, *Opt. Mater.*, 2020, **100**, 109631.

53 A. Ghosh, S. S. Dipta, S. S. S. Nikor, N. Saqib and A. Saha, Performance analysis of an efficient and stable perovskite solar cell and a comparative study of incorporating metal oxide transport layers, *J. Opt. Soc. Am. B*, 2020, **37**(7), 1966.

54 S. Ahmmed, A. Aktar, M. F. Rahman, J. Hossain and A. B. M. Ismail, A numerical simulation of high efficiency CdS/CdTe based solar cell using NiO HTL and ZnO TCO, *Optik*, 2020, **223**, 165625.

55 S. Sze and N. Kwok, *Physics of Semiconductor Devices*, Wiley-Interscience, 3rd edn, 2007.

56 S. M. Sze, C. R. Crowell and D. Kahng, Current transport in metal-semiconductor barriers, *J. Appl. Phys.*, 1964, **35**, 2534.

57 A. T. M. Islam, M. E. Karim, A. Rajib, Y. Nasuno, T. Ukai, S. Kurosu, M. Tokuda, Y. Fujii, Y. Nakajima, T. Hanajiri and H. Shirai, Chemical mist deposition of organic for efficient front- and back-PEDOT:PSS/crystalline Si heterojunction solar cells, *Appl. Phys. Lett.*, 2019, **114**, 193901.

58 A. Rajib, K. M. Enamul, S. Kurosu, T. Ukai, M. Tokuda, Y. Fujii, T. Hanajiri, R. Ishikawa, K. Ueno and H. Shirai, Synthesis of AlOx thin films by atmospheric-pressure mist chemical vapor deposition for surface passivation and electrical insulator layers, *J. Vac. Sci. Technol., A*, 2020, **38**, 033413.

59 M. J. Nayeen, B. K. Mondal, S. R. Basu and J. Hossain, Theoretical exploration of high V_{OC} in Cu_2SnS_3 TFSCss towards high efficiency, *Sol. Energy*, 2023, **265**, 112076.

60 A. Rahman M, Design and simulation of a high-performance Cd-free Cu_2SnSe_3 solar cells with SnS electron-blocking hole transport layer and TiO_2 electron transport layer by SCAPS-1D, *SN Appl. Sci.*, 2021, **3**(2), 253.

61 S. Paul, S. Grover, I. L. Repins, B. M. Keyes, M. A. Contreras, K. Ramanathan, R. N. Z. Zhao, F. Liao and J. V. Li, Analysis of Back-Contact Interface Recombination in Thin-Film Solar Cells, *IEEE J. Photovoltaics*, 2018, **8**(3), 871–878.

62 M. A. Rahman, Numerical modeling of ultra-thin $CuSbS_2$ heterojunction solar cell with TiO_2 electron transport and $CuAlO_2$:Mg BSF layers, *Opt. Mater. Express*, 2022, **12**(8), 2954–2972.

63 S. Demtsu and J. Sites, Effect of back-contact barrier on thin-film CdTe solar cells, *Thin Solid Films*, 2006, **510**(1–2), 320–324.

64 B. Ofuonye, J. Lee, M. Yan, C. Sun, J. M. Zuo and I. Adesida, Electrical and microstructural properties of thermally annealed Ni/Au and Ni/Pt/Au Schottky contacts on AlGaN/GaN heterostructures, *Semicond. Sci. Technol.*, 2014, **29**, 095005.

65 D. Zhaobin, F. Wu, Y. C. Wang and H. Jiang, Hong, Theoretical studies of the work functions of Pd-based bimetallic surfaces, *J. Chem. Phys.*, 2015, **142**, 214706.

66 D. Etor, M. Ekele and I. Akintunde, Impact of Metal Work-Function on Current Rectification by Metal-Insulator-Metal Diodes, *J. Eng. Technol.*, 2022, **7**(2), 430–434.

67 S. Sze and K. K. Ng, *Physics of Semiconductor Devices*, John Wiley and Sons, Inc., 1981.

68 P. Singh and N. Ravindra, Temperature dependence of solar cell performance-an analysis, *Sol. Energy Mater. Sol. Cells*, 2012, **101**, 36–45.

69 J. Li, H. Wang, M. Luo, J. Tang, C. Chen, W. Liu, F. Liu, Y. Sun, J. Hand and Y. Zhang, 10% Efficiency $Cu_2ZnSn(S,Se)_4$ TFSCss fabricated by magnetron sputtering with enlarged depletion region width, *Sol. Energy Mater. Sol. Cells*, 2016, **149**, 242–249.

70 M. Fathi, M. Abderrezek, F. Djahli and M. Ayad, Study of TFSCss in high temperature condition, *Energy Procedia*, 2015, **74**, 1410–1417.

71 A. B. Phillips, K. K. Subedi, G. K. Liyanage, F. K. Alfadhili, R. J. Ellingson and M. J. Heben, Understanding and advancing bifacial TFSCss, *ACS Appl. Energy Mater.*, 2020, **3**, 6072–6078.